

Grain refinement and solute distribution in Zircaloy-4 following high-pressure torsion

Siyu Huang^{1,2}, Levi Tegg^{1,2}, Sima Aminorroaya Yamini^{1,2}, Zhiyang Wang^{3,4}, Yi Huang^{5,6}, Limei Yang^{-5,7}, Ondrej Muránsky^{3,4}, Ingrid McCarroll⁸, Patrick A. Burr⁴, Julie M. Cairney^{*1,2}

¹ *Australian Centre for Microscopy and Microanalysis, The University of Sydney, Sydney, 2006, Australia*

² *School of Aerospace, Mechanical and Mechatronic Engineering, The University of Sydney, Sydney, 2006, Australia*

³ *Australian Nuclear Science and Technology Organisation (ANSTO), Sydney, 2232, Australia*

⁴ *School of Mechanical Engineering, University of New South Wales, Sydney, 2052, Australia*

⁵ *Department of Design and Engineering, Faculty of Science and Technology, Bournemouth University, Poole, Dorset BH12 5BB, UK*

⁶ *Materials Research Group, Department of Mechanical Engineering, University of Southampton, Southampton SO17 1BJ, UK*

⁷ *School of Civil & Environmental Engineering, University of Technology Sydney, Sydney, 2007, Australia*

⁸ *Max-Planck-Institut für Eisenforschung, Max-Planck-Str. 1, Düsseldorf, 40237, Germany*

* *corresponding author: julie.cairney@sydney.edu.au*

Abstract

Zirconium (Zr) alloys such as Zircaloy-4 are widely used for structural components and fuel cladding in industrial nuclear fission applications. High-pressure torsion (HPT), a severe plastic deformation process, produces an ultra-fine grain structure with properties that may have benefits in the nuclear industry, but the microstructural implications of processing of Zr alloys using this technique have not yet been extensively explored. Here, electron microscopy and atom probe tomography were used to investigate the microstructure and solute distribution in an as-received Zircaloy-4 and a fine-grained HPT-processed sample. Fe segregates to grain boundaries in both samples, however at much lower concentrations after HPT-processing, indicating that Fe diffuses to the newly formed grain boundaries during the severe plastic deformation. Although Sn segregates to the grain boundaries of the as-received sample, it is distributed almost homogeneously in the HPT-processed sample, which may provide advantages for corrosion resistance. Very low concentrations of Cr alloying elements at the matrix and grain boundaries of both samples is attributed to precipitation.

Keywords: Zircaloy-4, High-pressure torsion, Atom probe tomography, Solute segregation.

Zirconium (Zr) alloys are used for structural components and fuel cladding in the core of nuclear reactors because of their low neutron absorption cross-section and high corrosion resistance [1]. High-pressure torsion (HPT) is a severe plastic deformation method that subjects a thin disk-shaped sample to concurrent high pressure and torsional stress [2], resulting in grain refinement and potential phase transformations in many alloy systems [3, 4]. HPT can reduce grain sizes in Zr alloys to ~100 nm with high uniformity and stability [5, 6], and is being explored as a method to produce alloys with improved properties as a result of their unique structure. During service in reactors, Zr alloys experience a neutron flux that causes irradiation-induced damage, as well as high thermal and mechanical stresses that can lead to component deformation or failure. HPT introduces defects in the microstructure, including a very high density of grain boundaries [3, 7, 8], which may act as sinks for the irradiation-induced point defects. Therefore, it is thought that HPT can potentially enhance the tolerance to the irradiation damage of Zr alloys in service.

Metastable ω -Zr and β -Zr phases have been reported to form during HPT processing of Zr alloys [5, 6, 9, 10]. Similar grain structures were observed in Ti alloys that underwent severe plastic deformation, indicating that this could be a characteristic shared by materials with hexagonal close-packed (hcp) structures that have been treated at a low strain rate and ambient temperature [10].

The evolution of grains in severely deformed Zr alloys has been previously studied [3, 4, 7, 11], however, there are limited reports on changes in the chemical composition of HPT-processed Zr alloys. Understanding the distribution of solutes in Zr alloys between the matrix grains and boundaries is crucial for managing their in-reactor corrosion behaviour [12]. Here, the evolution of the microstructure and the distribution of solute atoms in an as-received plate of Zircaloy-4 is compared with the same alloy that has been processed by HPT, by using electron back-scatter diffraction (EBSD), transmission Kikuchi diffraction (TKD) and atom probe tomography (APT).

The as-received (hot-rolled and annealed) Zircaloy-4 plate has a nominal composition of Zr-1.56 Sn-0.22 Fe- 0.11 Cr (wt.%) [7]. A disc of 10 mm diameter and 0.8 mm thickness was prepared, oriented with the flat surfaces aligned to the original rolling direction. HPT was performed under 6.0 GPa

pressure at room temperature, with 10 revolutions at a rate of 1 rpm (designated as N10 in previous work [7]). Both samples were electropolished at room temperature using an electrolyte of 95% methanol and 5% perchloric acid at 30 V DC for EBSD analysis, performed by a Zeiss UltraPlus Scanning Electron Microscope. The as-received sample was sectioned into matchsticks and sharpened into sharp needles using two stages of electropolishing by conventional methods [13]. The electropolished needles were transferred to a Thermofisher G4 Hydra plasma focused ion beam (FIB) for annular milling and TKD analysis, in order to position a grain boundary near the specimen apex [14]. The HPT-processed specimens were prepared by the standard FIB lift-out and annular milling [15]. HPT-processed specimens were extracted from midway along the radius of the sample to avoid microstructural irregularities at the centre or periphery of the disc [7, 16]. TKD patterns of both samples were collected using an Oxford Instruments EBSD system using a 30 kV beam voltage. Patterns were analysed using Oxford Instruments HKL Tango software, where data was cleaned for wild spikes and 4 nearest neighbours. APT was performed using a Cameca LEAP4000X Si at a base temperature of 50 K, laser pulse energy of 100 pJ, pulse repetition rate of 200 kHz, and a target detection rate of 0.5%. Data was reconstructed and analysed using Cameca's Visualization and Analysis Software (AP Suite 6). The average evaporation field was set for Zr (28 V/nm), and the detector efficiency was 0.57. The AP Suite 6 default image compression factor 1.65 and k-factor 3.3 were used, as no poles were observed, and post-evaporation images were not collected to calibrate the reconstruction. Figure 1 shows the EBSD results from both the (a) as-received and (b) HPT-processed Zircaloy-4 samples, showing the inverse pole figure plot (IPF X) (note the scale difference). The grain sizes in the as-received sample range from 1 to 45 μm . The HPT-processed sample composed of predominantly nano-sized grains (~ 27 nm). Detailed EBSD analysis of these samples is reported elsewhere [7].

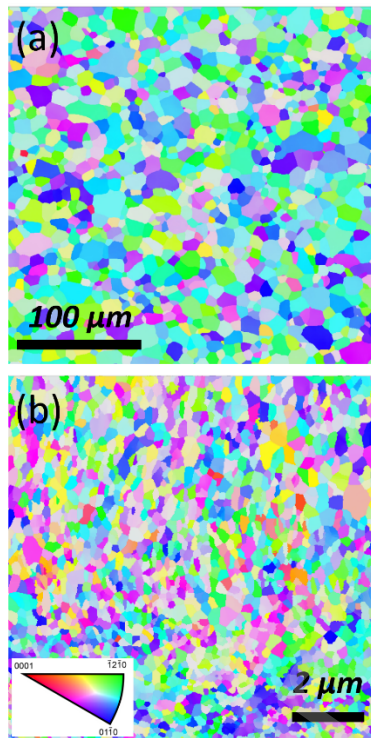


Figure 1. EBSD inverse pole figure (IPF X) orientation maps of the (a) as-received; and (b) HPT-processed samples, indicating significant reduction in grain size of the sample following HPT processing.

Figure 2 shows the site-specific FIB-milled specimens of the two specimens after annular milling, and correlated TKD data, used to locate the grain boundaries prior to the APT experiment.

Figure 2(a) and (e) show the secondary electron images of the tips from the as received and HPT samples, respectively, with the red boxes indicating the area analysed with TKD. Figure 2(b) to (d) show the band contrast (BC) map, IPF Y, and IPF Z of the region of interest, respectively, for the as-received sample. The grain boundary sits approximately 100 nm below the apex of the tip. Figure 2(f) to (h) show the BC map, IPF Y, and IPF Z data, respectively, for the HPT sample. Grain sizes at the apex vary from 30 to 100 nm, consistent with the EBSD results presented in Figure 1. Only α -Zr was detected in the mapping area. Previous reports noted that ω -Zr, which formed during HPT processing, reverted to α -Zr during TEM sample preparation by FIB milling [7]. The same milling method has been used in our study to prepare the APT tips and no evidence of ω -Zr phase was observed in the TKD, confirming the transformation of the metastable phase to α -Zr.

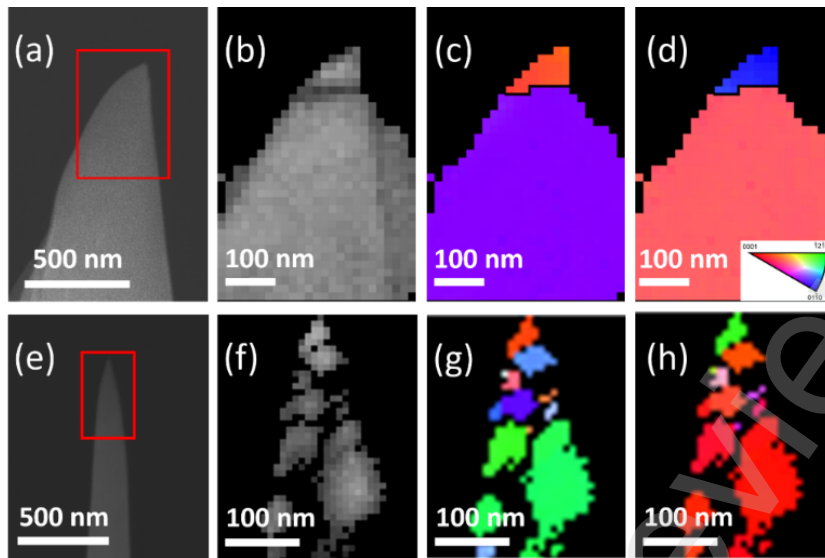


Figure 2. The SEM image and TKD results of as-received Zircaloy-4 sample: (a) SEM image, (b) BC map, (c) IPF Y, and (d) IPF Z; and HPT-processed sample: (e) SEM image, (f) BC map, (g) IPF Y, (h) IPF Z, following site-specific FIB milling.

Figure 3(a) shows an APT reconstructed volume showing the solute element positions (Fe, Al, Sn, Cr and Si) from the as-received sample (Figure 2(a)). A grain boundary is visible on the left and is enriched with Fe, Al and Cr, while Si appears to be randomly distributed. Si and Al are residual elements likely introduced to this alloy from raw materials used during casting. A region of interest (ROI) of $65 \text{ nm} \times 15 \text{ nm} \times 20 \text{ nm}$ was created (Figure 3(a)) to calculate a compositional profile normal to the grain boundary. Figure 3(b) and (c) show one-dimensional composition profiles of Fe, Sn, and Cr, Al. Fe is nearly absent in the α -Zr grains however, its concentration increases at the grain boundary to $\sim 3.5 \text{ at}\%$. Sn is dissolved in the Zr matrix with a concentration of $\sim 1.0 \text{ at}\%$, increasing to $\sim 2 \text{ at}\%$ near the grain boundary. There are also regions of higher Sn concentrations that extend along the z direction in the dataset due to field enhanced migration of Sn during APT analysis of the tip, causing artefacts in the reconstruction [17, 18]. Al and Cr show maximum concentrations of $\sim 0.03 \text{ at}\%$ and $0.2 \text{ at}\%$ at the grain boundary, respectively.

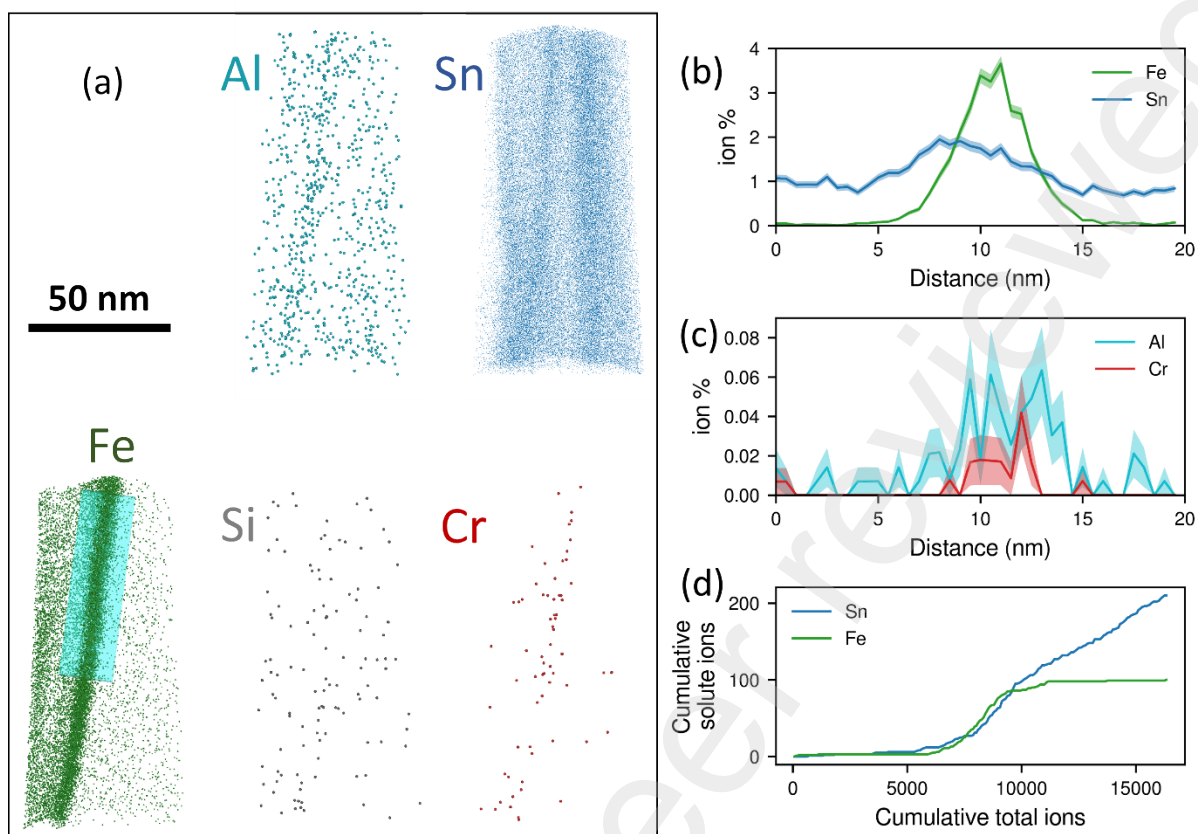


Figure 3. (a) APT reconstruction of the tip shown in Figure 2(a) from the as-received sample, the position of ROI to calculate the interfacial excess of solute atoms is shown in Fe reconstruction. Al, Cr, Si and Fe are rendered with spheres to enhance visibility. All reconstructed species are shown at the same magnification and from the same viewing angle; (b) concentration variation of Fe and Sn in the ROI shown in (a); (c) concentration variation of Al and Cr in the ROI shown in (a), the shaded area around the curves refers to the uncertainty of calculated values of concentrations, the composition analysis was performed in the direction normal to the grain boundary; (d) Cumulative profiles of Fe and Sn atoms detected across the grain boundary.

Care needs to be taken in interpretation of these compositions, especially the maximum measured concentration, as the boundary may not be perfectly perpendicular to the ROI, it may not be completely flat, and differences in evaporation field may result in trajectory aberrations. To quantify Fe and Sn segregation more accurately, cumulative compositional profiles were calculated from multiple smaller ROIs, normal to the grain boundary. An example cumulative profile of Fe and Sn from one of these ROI is shown in Figure 3(d). The average Gibbsian interfacial excess (Γ_i) [19] for Fe and Sn at this

grain boundary from these multiple ROIs is calculated to be $\Gamma_{\text{Fe}} = 0.52 \pm 0.04$ monolayers and $\Gamma_{\text{Sn}} = 0.28 \pm 0.18$ monolayers.

Figure shows the APT reconstruction of the tip prepared from the HPT-processed sample (Figure 2(e)) for Fe, Al, Cr, Si, Cu, and Sn. As for the as-received sample, Fe segregates to grain boundaries which are observed in the lower half of the reconstruction. The grain boundaries are annotated in Figure 4 to guide the eye. The data contains a grain boundary triple junction, and the three grain boundaries are labelled 'GB 1', 'GB 2' and 'GB 3'. Figure shows the segregation of Cu to the boundaries. This element was not detected in the as received sample. Cu, Si and Al are residual elements in this alloy and therefore their random distribution within the sample is expected.

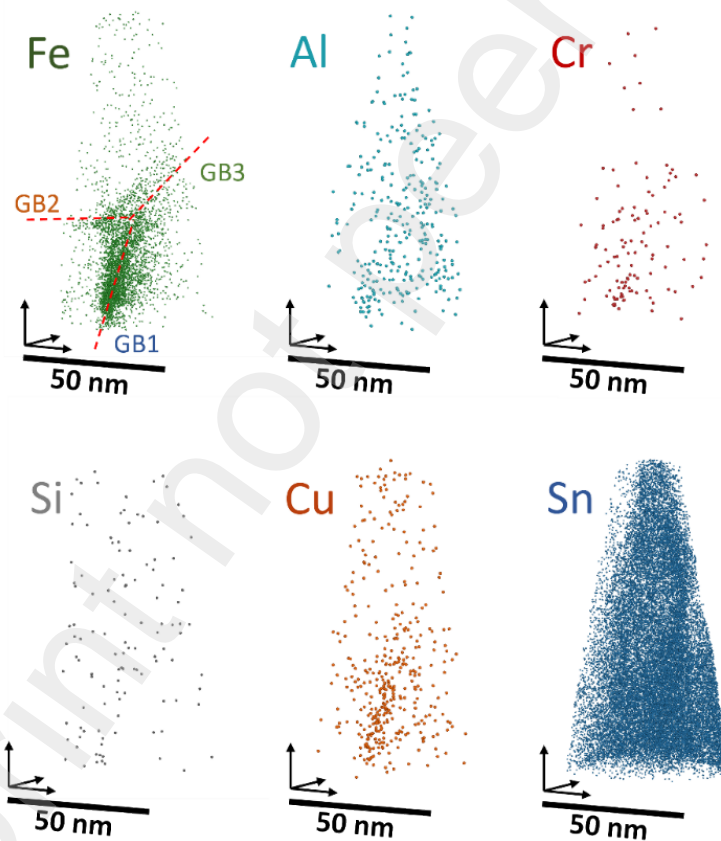


Figure 4. APT reconstruction of the tip shown in **Error! Reference source not found.**

Three cylindrical ROIs (10 nm diameter and 20 nm height) were positioned normal to each grain boundary to measure the composition of solute atoms at the boundary. Figure (a) show the variation in

concentration of Fe, Sn, Cr, and Al across three grain boundaries. Similar to the as-received sample, Fe is nearly absent in the α -Zr matrix, but is enriched at the three grain boundaries, reaching peak concentrations of ~ 1.8 at% at GB 1, ~ 0.9 at% at GB 2, and ~ 0.5 at% at GB 3. The concentration of Sn doesn't vary significantly between the matrix and grain boundaries, which is consistent with the ion distribution shown in Figure . Al shows no measurable enrichment at grain boundaries. Due to the very low number of Cr and Al atoms detected at the grain boundaries, the relative uncertainty of the measured values is high. This analysis indicates that residual atoms of Al, Si and Cu are present at very low concentrations in this alloy and distributed randomly within the grain and grain boundaries of the HPT-processed sample. Concentrations of these elements are too low to have meaningful segregation analysis. The Gibbsian interfacial excess of the Fe was calculated from cumulative compositional profiles determined for three random smaller cuboid ROIs ($5 \text{ nm} \times 5 \text{ nm} \times 20 \text{ nm}$) for GB 1, GB 2 and GB 3, all normal to the grain boundaries. Figure 5(b) shows example cumulative profiles of Fe atoms detected across the three grain boundaries. Γ_{Fe} values at the different grain boundaries are $\Gamma_{\text{Fe}}(\text{GB1}) = 0.28 \pm 0.15$, $\Gamma_{\text{Fe}}(\text{GB2}) = 0.039 \pm 0.008$, and $\Gamma_{\text{Fe}}(\text{GB3}) = 0.06 \pm 0.01$ monolayers. The Γ_{Fe} for the as-received sample was 0.52 ± 0.04 monolayers, which is much higher than for the HPT-processed sample, suggesting redistribution of Fe during the severe plastic deformation.

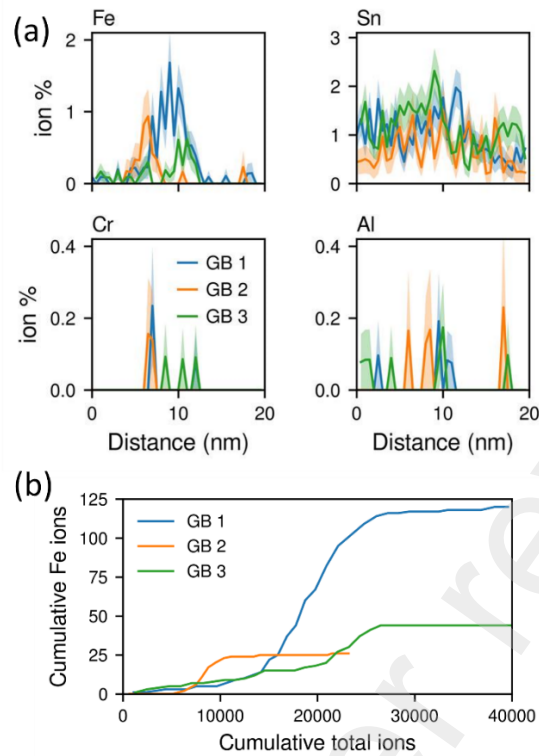


Figure 5. (a) 1D concentration profiles of elements across the ROI normal to the grain boundaries shown in Figure 5 for Fe, Sn, Cr, and Al. The shaded regions around the lines represent uncertainties of the analysis; (b) Cumulative profiles of Fe atoms detected across the grain boundaries (GB 1, 2 and 3) in the HPT-processed sample. Cuboid regions with equal length crossed both grains perpendicular to the interfaces.

The alloying element Sn in Zircaloy-4 can dissolve in the Zr matrix, while Fe and Cr are predominantly found in the $Zr(Cr,Fe)_2$ Laves precipitates [20]. The low concentration of Fe observed in the matrix (0.022 at%) in the as-received sample is consistent with the Zr-Fe phase diagram [21]. This alloy has undergone hot rolling and stress-relief annealing, resulting in an exceptionally low content of Fe in α -Zr [22]. Fe has previously been detected at grain boundaries in Zr alloys [20, 23-26]. Similarly, our results indicate that Fe can segregate to the grain boundaries at concentrations higher than the equilibrium Fe solubility (120 wt ppm at 800 °C and less than 50 wt ppm <300°C [21]) in the α -Zr matrix without forming precipitates (Figures 3 and 5). However, the HPT-processed sample contains less Fe segregation at grain boundaries than the as-received sample. The Fe at the newly-generated grain boundaries can only originate from the original grain boundaries or from second phase particles (mostly Laves phase). A previous synchrotron X-ray diffraction study [7] of Zircaloy-4 showed no significant changes in the peak intensities of second phase particles (SPPs) after the HPT processing, suggesting

that the dissolution of SPPs does not occur during HPT. The decrease in concentration of Fe at the grain boundaries following HPT is therefore attributed to the redistribution of Fe from the original boundaries throughout the newly formed interfaces and dislocation sites.

As a qualitative approximation, in dilute alloy systems, high angle grain boundaries have been shown to have greater levels of solute segregation than low angle boundaries [27, 28], though the temperature and presence of other solutes in a multicomponent system strongly affect the solute enrichment factor at the grain boundaries [27]. The three grain boundaries we analysed in the HPT-processed sample exhibit differing concentrations of solutes (Figure 5(a)) and the differences are most dramatic for Fe. HPT processing has increased the surface area of grain boundaries significantly (Figure 1). Several high and low-angle grain boundaries are observed within 200 nm of the atom probe tip prepared from the HPT-processed sample (Figure 2(f) to (h)). The much higher concentration of Fe at GB1 relative to GB2 and GB3 is thought to be due to differences in the nature of the boundaries, where GB1 is likely to be a high-angle boundary and the other two boundaries are thought to be low angle boundaries.

Despite a low concentration of Cr in both the matrix and the grain boundaries, Cr enrichment was visible in both samples (Figures 3(c) and 5(c)). This alloy nominally contains 0.11 wt% Cr, half of the nominal composition of Fe. The tendency of solute segregation is inversely related to its bulk solubility [27]. Segregation of Cr to grain boundaries is reported in quenched sample of binary Zr-0.15 wt% Cr alloy [26] and Zr-Fe-Cr alloys [29]. The Cr concentration is too low for a meaningful segregation quantification, as the measured difference is within the range of uncertainty. Previous work [26] also noted the formation of spherical particles by Cr at the grain boundaries of a quenched sample (referred to as segregation); these might be nuclei of precipitates if the sample was further annealed. The regions we analysed contained much more Fe than Cr (much more than double), suggesting that the Cr in this alloy is mostly consumed by Cr-rich precipitates, such as the $Zr(Fe,Cr)_2$ Laves phase [30].

Interestingly, Sn clearly segregates to the grain boundaries of the as-received Zircaloy-4 but appears homogeneously distributed in the HPT-processed sample. Lower Sn segregation at the grain boundaries benefits the strength of the alloy [31], so Sn segregation to grain boundaries in Zr alloys has been

extensively studied [20, 24, 31-33], but findings are inconsistent. Some studies argue that Sn segregation observed at grain boundaries is related to the known artefacts linked to the field-enhanced migration of Sn [17, 18]. We do not believe that is the case here, as the boundary lies at an angle to the long axis of the reconstruction and can be observed separately to the field induced migration. Sn segregation has not been observed in ZIRLO [25], however, studies report Sn segregation at the grain boundaries of Zircaloy-2 [32], Zircaloy-4 [20], and CZ1 [24]. Grain boundary segregation of Sn was not evident in the HPT sample, but variations in the Sn concentration can be seen across the dataset (Figure 5), so field induced migration may be clouding the observations. The very small grain sizes and highly distorted structure of the matrix from severe deformation probably also affect the migration of Sn during field evaporation. So, while we observe that severe deformation reduces Sn segregation (potentially advantageous for mechanical properties), further work is required to confirm this effect.

In summary, Zircaloy-4 forms ultra-fine grains after the HPT processing. Fe, Cr, and Al segregate at the grain boundaries in both as-received and HPT-processed samples. Sn is segregated to the grain boundary in the as-received sample, but we did not find such clear evidence of segregation in HPT-processed samples. Cr segregates at boundaries but is only observed at very low concentrations. This element has extremely low solubility in Zr alloys and is thought to be consumed to form precipitates. Residual elements of Si and Cu were detected in some grains and grain boundaries. The concentration of Fe at grain boundaries of the as-received sample is much higher than that of HPT-processed sample due to the increase in available grain boundary area in the HPT sample to accommodate Fe atoms. Fe concentration varies considerably between grain boundaries in the HPT-processed sample, most likely due to different grain boundary structures (low angle vs higher angle boundaries).

Acknowledgements

This work was supported by the Australian Research Council (ARC) grants FT180100232 and IM230100125. The authors acknowledge the technical and scientific support provided by Sydney Microscopy and Microanalysis at the University of Sydney, and the support of Microscopy Australia.

Reference

- [1] A.T. Motta, L. Capolungo, L.Q. Chen, M.N. Cinbiz, M.R. Daymond, D.A. Koss, E. Lacroix, G. Pastore, P.C.A. Simon, M.R. Tonks, Hydrogen in zirconium alloys: A review, *J. Nucl. Mater.* 518 (2019) 440-460.
- [2] N. Smirnova, V. Levit, V. Pilyugin, R. Kuznetsov, L. Davydova, V. Sazonova, Evolution of the structure of fcc single crystal subjected to strong plastic deformation, *Fiz. Metal. Metalloved* 61 (6) (1986) 1170.
- [3] Z. Yu, S. Jin, M. Feng, M.Y. Murashkin, R.Z. Valiev, S.P. Ringer, G. Sha, Temperature-dependent composition of η phase in an Al-Zn-Mg-Cu alloy under high pressure torsion: Kinetics and thermodynamics, *Acta Materialia* 237 (2022) 118181.
- [4] M. Stückler, H. Krenn, P. Kürsteiner, B. Gault, F. De Geuser, L. Weissitsch, S. Wurster, R. Pippan, A. Bachmaier, Intermixing of Fe and Cu on the atomic scale by high-pressure torsion as revealed by DC-and AC-SQUID susceptometry and atom probe tomography, *Acta Materialia* 196 (2020) 210-219.
- [5] M.T. Pérez-Prado, A. Gimazov, O.A. Ruano, M. Kassner, A. Zhilyaev, Bulk nanocrystalline ω -Zr by high-pressure torsion, *Scripta Mater.* 58 (3) (2008) 219-222.
- [6] Y. Wang, M. Louie, Y. Cao, X. Liao, H. Li, S. Ringer, Y. Zhu, High-pressure torsion induced microstructural evolution in a hexagonal close-packed Zr alloy, *Scripta Mater.* 62 (4) (2010) 214-217.
- [7] L. Chen, Z. Wang, H. Zhu, P.A. Burr, J. Qu, Y. Huang, L. Balogh, M. Preuss, O. Muránsky, On the microstructure and high-temperature stability of nano-grained Zircaloy-4, *Scripta Mater.* 210 (2022) 114410.
- [8] R. Harsha, V.M. Kulkarni, B.S. Babu, Severe plastic deformation-a review, *Materials Today: Proceedings* 5 (10) (2018) 22340-22349.
- [9] A.P. Zhilyaev, A.V. Sharafutdinov, M.T. Pérez-Prado, Phase Transformations During High-Pressure Torsion of Pure Zr and of a Zr-2.5% Nb Alloy, *Adv. Eng. Mater.* 12 (8) (2010) 754-757.
- [10] R. Haraguchi, Y. Yoshimatsu, T. Nagaoka, M. Arita, K. Edalati, Z. Horita, Electrical resistivity mapping of titanium and zirconium discs processed by high-pressure torsion for homogeneity and phase transformation evaluation, *J. Mater. Sci.* 52 (2017) 6778-6788.
- [11] X. Sauvage, G. Wilde, S. Divinski, Z. Horita, R. Valiev, Grain boundaries in ultrafine grained materials processed by severe plastic deformation and related phenomena, *Mater. Sci. and Eng.: A* 540 (2012) 1-12.
- [12] B. Cox, Some thoughts on the mechanisms of in-reactor corrosion of zirconium alloys, *J. Nucl. Mater.* 336 (2-3) (2005) 331-368.
- [13] B. Gault, M.P. Moody, J.M. Cairney, S.P. Ringer, *Atom probe microscopy*, Springer Science & Business Media, 2012.
- [14] K. Babinsky, R. De Kloe, H. Clemens, S. Primig, A novel approach for site-specific atom probe specimen preparation by focused ion beam and transmission electron backscatter diffraction, *Ultramicroscopy* 144 (2014) 9-18.
- [15] M.K. Miller, K.F. Russell, Atom probe specimen preparation with a dual beam SEM/FIB miller, *Ultramicroscopy* 107 (9) (2007) 761-766.
- [16] X. An, S. Wu, Z. Zhang, R. Figueiredo, N. Gao, T. Langdon, Evolution of microstructural homogeneity in copper processed by high-pressure torsion, *Scripta Mater.* 63 (5) (2010) 560-563.
- [17] J. Wei, P. Frankel, E. Polatidis, M. Blat, A. Ambard, R. Comstock, L. Hallstadius, D. Hudson, G. Smith, C. Grovenor, The effect of Sn on autoclave corrosion performance and corrosion mechanisms in Zr-Sn-Nb alloys, *Acta Materialia* 61 (11) (2013) 4200-4214.
- [18] D. Hudson, A. Cerezo, G.D. Smith, Zirconium oxidation on the atomic scale, *Ultramicroscopy* 109 (5) (2009) 667-671.
- [19] M.K. Miller, *Atom probe tomography: analysis at the atomic level*, Springer Science & Business Media, 2012.
- [20] Y. Dong, A.T. Motta, E.A. Marquis, Atom probe tomography study of alloying element distributions in Zr alloys and their oxides, *J. Nucl. Mater.* 442 (1-3) (2013) 270-281.
- [21] C.-C. Wei, A. Aitkaliyeva, Z. Luo, A. Ewh, Y.H. Sohn, J.R. Kennedy, B.H. Sencer, M.T. Myers, M. Martin, J. Wallace, M.J. General, L. Shao, Understanding the phase equilibrium and irradiation effects in Fe-Zr diffusion couples, *Journal of Nuclear Materials* 432 (1) (2013) 205-211.
- [22] H. Zou, G. Hood, J. Roy, R. Schultz, J. Jackman, The solid solubility of Fe in α -Zr: a secondary ion mass spectrometry study, *J. Nucl. Mater.* 210 (3) (1994) 239-243.
- [23] J. Eriksson, G. Sundell, P. Tejlund, H.-O. Andrén, M. Thuvander, Nanoscale chemistry of Zircaloy-2 exposed to three and nine annual cycles of boiling water reactor operation—an atom probe tomography study, *J. Nucl. Mater.* 561 (2022) 153537.
- [24] W. Lin, Q. Lv, D. Jiao, L. Zhang, J. Tan, G. Sha, J. Hu, Creep-induced redistribution of alloying elements in CZ1 zirconium alloys, *J. Mater. Sci. Tech.* 173 (2024) 31-44.
- [25] D. Hudson, G.D. Smith, Initial observation of grain boundary solute segregation in a zirconium alloy (ZIRLO) by three-dimensional atom probe, *Scripta Mater.* 61 (4) (2009) 411-414.
- [26] B. Gault, P.J. Felfer, M. Ivermark, H. Bergqvist, J.M. Cairney, S.P. Ringer, Atom probe microscopy characterization of as quenched Zr-0.8 wt% Fe and Zr-0.15 wt% Cr binary alloys, *Mater. Lett.* 91 (2013) 63-66.

- [27] S. Hofmann, P. Leiček, Solute segregation at grain boundaries, *Interface Sci.* 3 (4) (1996) 241-267.
- [28] X. Zhou, X.-x. Yu, T. Kaub, R.L. Martens, G.B. Thompson, Grain Boundary Specific Segregation in Nanocrystalline Fe(Cr), *Sci. Rep.* 6 (1) (2016) 34642.
- [29] P.A. Burr, M.R. Wenman, B. Gault, M.P. Moody, M. Ivermark, M.J.D. Rushton, M. Preuss, L. Edwards, R.W. Grimes, From solid solution to cluster formation of Fe and Cr in α -Zr, *J. Nucl. Mater.* 467 (2015) 320-331.
- [30] A.W. Aldeen, Z.W. Chen, I.A. Disher, M. Samiuddin, K. Yan, Second Phase Particles in Zr–Sn–Nb–Fe Alloys: A Review, *Phys. Met. Metallogr.* 124 (4) (2023) 362-379.
- [31] Z. Xue, X. Zhang, J. Qin, M. Ma, R. Liu, Exploring the effects of solute segregation on the strength of Zr $\{101\bar{1}\}$ grain boundary: A first-principles study, *J. Alloys Compd* 812 (2020) 152153.
- [32] T. Sawabe, T. Sonoda, Evolution of nanoscopic iron clusters in irradiated zirconium alloys with different iron contents, *J. Nucl. Sci. Technol.* 55 (10) (2018) 1110-1118.
- [33] R. Yuan, Y.-P. Xie, T. Li, C.-H. Xu, M.-Y. Yao, J.-X. Xu, H.-B. Guo, B.-X. Zhou, An origin of corrosion resistance changes of Zr alloys: effects of Sn and Nb on grain boundary strength of surface oxide, *Acta Materialia* 209 (2021) 116804.